Multiscale model of near-spherical germanium quantum dots in silicon*

D T Read and V K Tewary

Materials Reliability Division, National Institute of Standards and Technology, Boulder, CO 80305, USA

E-mail: read@boulder.nist.gov

Abstract

Atomic displacements, strains and strain energies in the neighbourhood of near-spherical, coherent Ge 'quantum dots' (QD) in crystalline Si and near a {001} Si surface have been predicted by multiscale modelling, by use of a combination of classical molecular dynamics (MD) and Green's function (GF) techniques. The model includes the nonlinear effects at the GeSi interface and allows the boundary of the system to be placed outside the two million atom host crystallite. A modified-embedded-atom-model interatomic potential was used for both MD and GF calculations. Dots of four sizes were analysed, ranging in diameter from 1.1 to 6.5 nm. The supercell size was 34.2 nm. Calculations for strains and displacements in the infinite solid were extended to the {001} surface of the semi-infinite solid using the scheme described previously. Atomic displacements in the infinite solid showed trends generally similar to the early estimate of Mott and Nabarro, but differed in detail, especially for the smaller dots. Surface displacements were broadly similar in magnitude and shape to the classic isotropic continuum solution of Mindlin and Cheng. For large (e.g. 6.5 nm diameter) near-surface dots, the surface displacements are of a magnitude sufficient to be observed by advanced scanned probe microscopy.

1. Introduction

1.1. Motivation

Quantum dots (QD) are candidate structures for the active elements in many revolutionary new devices including quantum computers, which may have processing capabilities vastly greater than even today's extremely sophisticated billion-transistor complementary metal oxide semiconductor (CMOS) structures [1]. Quantitative understanding, including modelling and measurement, of strains around quantum dots is important because carrier confinement, which is responsible for the energy levels of quantum dots, is determined by: (i) dot geometry; (ii) chemical composition of the dot and its surroundings; and (iii) the mismatch-induced elastic strains around the dot [2]. In self-assembled dots, the strain affects the dot geometry and chemical composition. So the mismatch-induced strains are fundamental to both the formation and

the performance of solid state quantum dots [3–5]. Strain engineering in quantum dots has been reported for controlling the self-assembly of quantum dot arrays and has been used to demonstrate the effect of strain on the energy of emitted photons. The performance of a QD for quantum information processing or for generation of light can obviously be affected by strains in and around the dot, in particular, as they affect decoherence of the quantum states used to store and manipulate information [6, 7].

Experimental images of surface topography can, in principle, be used to characterize QD size, spacing and in-plane location. Quantitative models of displacements and strains observable at the surface above buried QD offer the possibility of using quantitative experimental measurements of surface parameters to produce more exact values for size, spacing and location, and to extract additional useful information. There may be useful information in, for example, a quantitative map of the out-of-plane displacement at and near a buried QD to extract some important characteristics of the QD such as an effective lattice misfit. However, quantitative interpretation

---

1

of the experimental results is difficult because of the alloying and other effects that occur during spacer layer deposition. These effects depend upon the experimental conditions and the sample history. On the other hand, model calculations of strain and displacement field due to an idealized QD can provide valuable insight into the physical processes and are useful in the design of experiments. Clearly, models for a range of shapes and sizes will be needed, because quantum dots of a variety of shapes have been reported experimentally.

The key contribution of this paper is an analysis approach that combines a full atomistic treatment of the QD and its interface to the host lattice with a correct treatment of the boundary conditions. To demonstrate the approach, we consider faceted polyhedral (near-spherical) QD of a range of sizes, although the modelling approach developed here is applicable to QD of any arbitrary shape. Treatment of spherical or near-spherical shapes allows comparisons with closed-form expressions based on continuum mechanics, and also allows exploration of general behaviour not influenced by the asymmetries of a particular shape. The largest diameter analysed here, 6.5 nm, is within the range of observed QD sizes for GeSi [8] and Ge–silica [9] systems. In general the experimentally observed QDs are more like pyramids or truncated pyramids [8]. However, it is important to establish a correct, as opposed to arbitrary, treatment of the boundary conditions and to have a good understanding of how atomistic results for the spherical QD compare to continuum approximations before proceeding on to more complex shapes.

This paper is focused on three aspects of the near-spherical Ge–Si QD: the positions of the atoms near the Ge–Si interface, the surface distortions produced by buried QD and the strain at the surface above a buried QD. The atomic positions are critical for calculation of the electronic–photonic behaviour of the QD. The surface distortions are potentially useful for relating scanned-probe microscopy (SPM) observations to certain features of buried QD. And the surface strains provide an indication of which positions may be favourable for formation of neighbouring dots in self-assembled arrays.

1.2. Multiscale approach

Modelling of strains in and around quantum dots is a key tool in strain engineering of QD. However, the modelling of these strains is complicated by the large number of atoms that must be considered in order to treat quantitatively the effects of the QD-matrix interaction. Both multiscale and direct approaches to modelling strain around QD have been reported in the literature. The direct approaches include continuum elasticity, e.g. [10], Green's function (GF) [11, 12] and molecular dynamics (MD) [13–17] approaches. The multiscale approaches so far include MD and finite element (FE) combinations [18] and MD and GF combinations [19, 20]. Our model systems are similar in size to those reported by Makeev and Madhukar [17], except that our models are as large in the [001] direction, perpendicular to the free surface of the Si host, as in the other directions. We used a different potential; our germanium quantum dots are faceted according to the Wigner–Seitz symmetry; and we used much more modest computational resources. Our results show some features not seen in [17].

Here we apply the multiscale approach that incorporates MD and GF [19]. We take advantage of the fact that, away from the QD, the strains are relatively small, that is, small enough that the harmonic approximation is accurate. These far-field strains provide the boundary condition for the QD, and so cannot be ignored. Treating the far field in a harmonic approximation, by use of the Green's function approach, is a much more efficient use of computer power than a full MD treatment would be [19, 20]. We note that the GF is itself multiscale, allowing a seamless transition between an atomistic treatment of a *perfect*, harmonic lattice (LGF) and a continuum with infinitesimal strain (CGF). Therefore our approach is multiscale over three different scales: nonlinear atomistic, in the MD region; linear atomistic, in the LGF region; and continuum, in the CGF region. A similar multiscale approach has been used previously [21] to model single Ge impurities and their aggregates in Si. That approach does not include nonlinear effects, and is based on a numerical calculation of the Green's function using Tersoff's [22] potential for Si. We used the present approach to model Au nanoislands in Cu using a different interatomic potential [19].

In the case of QDs of realistic sizes, it is necessary to model a large host crystallite in order to avoid spurious size effects that might be introduced by arbitrarily assumed boundary conditions. It is also necessary to include nonlinear effects inside and near QDs because of large atomic displacements in these regions. Our multiscale model is computationally efficient and accounts for these nonlinear effects as well as models a large crystallite without being CPU intensive. In the present calculations we are able to model a QD as large as 6.5 nm and include 2 million atoms in the host crystallite on a desktop computer.

One mathematical problem in linking the lattice scale to the continuum scale is that the discrete lattice model yields atomic displacements at discrete lattice points. On the other hand, stress and strain are continuum model parameters. They are continuous variables and are defined in terms of the derivatives of the displacement field. In the continuum model these derivatives are uniquely defined because the displacement field is a continuous variable. In the lattice model the displacement field is a discrete variable and a numerical algorithm and an averaging process are needed to define the derivatives. Although elegant averaging techniques [23] have been developed for this purpose in infinite solids, the averaging process is not unique and requires careful attention to convergence as well as various conservation laws, particularly in models containing a free surface. This problem does not arise in our multiscale model because the lattice Green's function reduces seamlessly [24] to the continuum Green's function from which stress and strain can be uniquely determined.

The details of our multiscale model have been given in [19, 24]. Here we shall present a brief summary and the salient features of our model. We consider the quantum dot as a defect in an otherwise perfect lattice. The defect causes lattice distortion by displacing each atom in the lattice from its position of equilibrium. The displacement field **u** in the entire lattice can be written [24, 25] as

$$\mathbf{u} = \mathbf{G}^*\mathbf{F}, \tag{1}$$

where $\mathbf{G}^*$ is the defect Green's function [25] of the lattice containing the defect. It is related [25] to the perfect lattice Green's function $\mathbf{G}$ (for the host lattice without the defect) through the Dyson equation [26]:

$$\mathbf{G}^* = \mathbf{G} + \mathbf{G}\mathbf{\Delta\Phi}(\mathbf{u})\mathbf{G}^*, \qquad (2)$$

where $\mathbf{\Delta\Phi}$ denotes the change in the lattice force constants caused by the defect. All the quantities in equations (1) and (2) are matrices in the vector space defined by all the lattice sites. $\mathbf{G}$, $\mathbf{G}^*$ and $\mathbf{\Delta\Phi}$ are square matrices and $\mathbf{u}$, $\mathbf{F}$ and $\mathbf{F}^*$ are column matrices. In the harmonic approximation $\mathbf{\Delta\Phi}$ is independent of $\mathbf{u}$. In this case equation (2) can be solved by standard methods [25, 26].

As shown in [19, 24, 25], we can rewrite equation (1) in the following exactly equivalent form

$$\mathbf{u} = \mathbf{G}\mathbf{F}^*, \qquad (3)$$

where

$$\mathbf{F}^* = \mathbf{F} + \mathbf{\Delta\Phi}(\mathbf{u})\mathbf{u}. \qquad (4)$$

The effective force $\mathbf{F}^*$ is known as the Kanzaki force [27]. Physically it can be interpreted as the force due to the defect at the displaced positions of the atoms. The Kanzaki force contains the full contribution of the discrete structure of the lattice in the defect space as well as nonlinear effects.

As shown in [24, 25], $\mathbf{G}$, but not $\mathbf{G}^*$, reduces asymptotically to the continuum Green's function. Equation (3) forms the basis of our multiscale model. We first calculate $\mathbf{F}^*$ by using an iterative procedure described below. This method is based upon the use of the standard MD and the lattice Green's function method [25]. We calculate the displacements near the defect from equation (1) by using the lattice Green's function. At large distances from the defect, we replace $\mathbf{G}$ by $\mathbf{G}_\mathrm{c}$, the continuum Green's function [28], but still use the lattice value of $\mathbf{F}^*$ given by equation (4). Equation (3) thus relates the discrete lattice parameters through $\mathbf{F}^*$ to the continuum model parameters through $\mathbf{G}_\mathrm{c}$. We incorporate the effect of extended defects in $\mathbf{G}_\mathrm{c}$ by imposing appropriate boundary conditions using the standard [28] techniques of the continuum model.

Prospective applications of (1) are manifold. For example, dislocations and other local defects within or at the boundary of the Ge QD can be included within the inner core region, since MD accommodates such geometries and can be used to produce a set of Kanzaki forces representative of the QD with dislocations. Using this approach, the effect of dislocations or other features of the QD structure on the strains surrounding the QD could be modelled [29].

To model observable effects of the QD, a surface is introduced in the continuum region using the technique described previously [24]. The technique of Mindlin is used with the Kanzaki forces [25] and the continuum Green's function to calculate the additional image forces that are needed to model the effect of the surface. Here we have not accounted for the effect of the surface on the Kanzaki forces. This introduces a small error into our results for surface strains and displacements, which is not expected to affect our general conclusions.

1.3. Interatomic potential

The GF and MD regions of our multiscale model use the same interatomic force model. We have chosen the modified embedded atom model (MEAM) [30], because it is realistic for Si, Ge and their alloys, and is practical. However, our model is not limited to this particular potential. Any differentiable potential function can be used, from which force constants can be obtained numerically or analytically. The force constants are needed for calculation of the lattice Green's function.

Equation (9) of [30], for the background electron density, allows negative values inside the square root for certain nonequilibrium, but very possible, atomic arrangements; we use instead equation (12c), introduced in [31] and discussed further in [32]. The parameters originally given in [30] were adjusted to best fit the modified potential to the elastic moduli, vacancy energy, and energy and volume of metastable crystal structures of Si and Ge [33–36]. (Fits to the sublimation energy and lattice parameter are built in to the MEAM potential.) We followed the prescription given in the original [30] to derive parameters for the Si–Ge interaction. The MEAM parameters used here for Si–Si, Si–Ge and Ge–Ge interactions are listed in table A.1 of the appendix. The screening and distance cutoffs ensured that, for configurations near equilibrium, only the interactions with the four nearest neighbours were calculated explicitly. Interactions of an atom with its more distant neighbours are indirect, through the background electron density. The MD calculations used the XMD computer program, described by Rifkin [37], significantly modified by the addition of the MEAM potential.

The GF is based on this same interatomic potential, except that only Si–Si interactions occur in the GF region of the problem. The GF was built up by the procedure described in [24] from numerical force derivatives calculated from the present potential function. The force constant matrices used here are given explicitly in the appendix.

1.4. General procedure and outline of the paper

Our objective is to find the correct set of Kanzaki forces and then apply them to calculate certain quantities of interest for the Ge–Si QD. The configurations to be treated are described in section 2. An iterative scheme to calculate the Kanzaki forces is outlined in section 3. In section 4, the Kanzaki forces are utilized to calculate: boundary conditions used in an MD calculation of atomic positions at the Ge–Si interface; atomic displacements along principal directions around a Ge–Si QD in an infinite solid; and strains and displacements at a surface near the QD. Section 5 compares our approach and results to previous models of the Ge–Si QD.

2. Model configurations

We have analysed the Ge–Si QD as a Ge inclusion in a Si host lattice. Our nomenclature is shown in figure 1. The QD is contained within a supercell with full Wigner–Seitz face-centred-cubic symmetry. The supercell boundaries remain fixed throughout the solution procedure. The supercell diameter is 34.2 nm. Therefore we expect to obtain good accuracy for atomic displacements and derived quantities up to a distance of about 17 nm from the centre of our QD. By this distance, the displacements and strains are very small. The
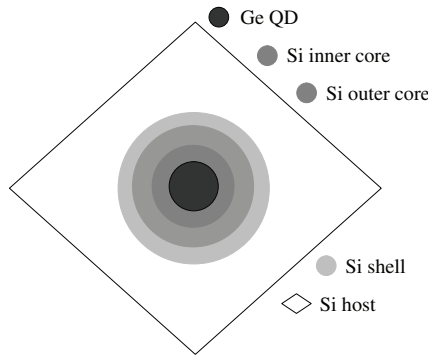
Figure 1. Schematic diagram of a Ge–Si quantum dot, showing regions considered in the multiscale analysis. The MD and GF solutions are joined by matching forces at each atom in the shell region.
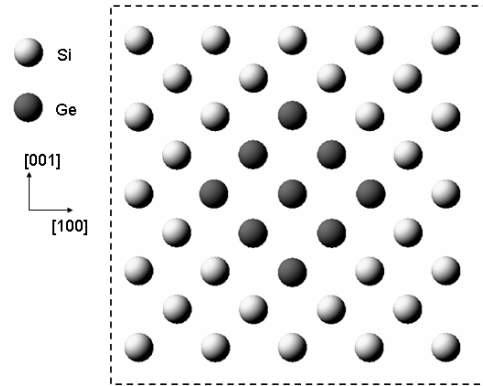

Figure 2. Section through the [010] plane of quantum dot size A, showing facets. Only atoms near the QD are shown; the full model is much larger.

Figure 3. Section through the [010] plane of quantum dot size F, showing that this QD is nearly spherical. Only atoms near the QD are shown; the full model is much larger.

Kanzaki forces, which occur near the centre of the supercell and therefore are considered to be unaffected by the cell boundary, are used to evaluate displacements and strains at much larger distances.

Our Ge QD are built up by including Wigner–Seitz unit cells out to spherical cutoffs, to preserve the symmetry of the lattice. For this demonstration analysis the QD has the full tetrahedral symmetry, but this is not required by the method. This scheme produces faceted polyhedral Ge QD, which become more nearly spherical as the size increases. Our smallest QD is definitely faceted, and our largest inclusion is nearly spherical, see figures 2 and 3. We report on four inclusion sizes, which are referred to below as A, B, C and F. The diameters and atom counts are given in table 1. The largest size described here, size F, contains 7193 Ge atoms, for a QD diameter of about 6.5 nm. The shell, where the force balance between the GF and MD sides of the problem occurs, consists of 7796 Si atoms. This size was chosen because it is large enough to be physically realistic but still small enough to be modelled with tractable calculation times; the smaller sizes were chosen to look for the possibility of size effects. Throughout the calculation, we used the Cartesian coordinate system with axes aligned along the crystallographic axes.

3. Analysis

3.1. Approach

We have developed and applied an iterative scheme to calculate the needed Kanzaki forces. In this problem the Kanzaki forces represent, in a somewhat complex fashion to be discussed below, the force exerted by the QD and its surrounding atoms, out to the core, on the shell and the host atoms, as defined in figure 1. The Ge lattice is larger than that of Si, so the QD expands against the restraining force of the surrounding atoms. The shell is the transition or 'handshake' region between the MD and GF portions of the analysis; the shell atoms remain fixed during each MD analysis. It is straightforward to use MD to calculate the outward force on the shell atoms, but the result depends on the position of the shell atoms. The shell atoms can be displaced using (1), once we have a set of forces. Iteration is required because we must first use (1) to displace the shell atoms, and then repeat the MD calculation to refine the force values.
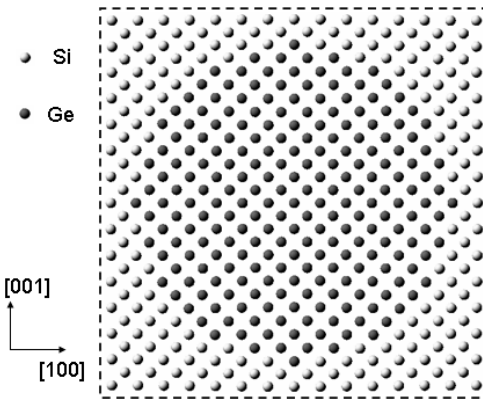
The subtlety of the plan outlined above is that the Kanzaki forces must be applied to the perfect Si lattice, even though the configuration of interest is different, namely the Ge–Si QD. As indicated by (1), it is possible to choose the Kanzaki force values to account for this difference between $\mathbf{G}^*$ and $\mathbf{G}$. Figure 4 shows simplified force balance diagrams from two configurations of atoms, one representing a physical configuration of interest, in this case a Ge–Si QD, the other a perfect Si lattice (PL).

In the QD there are no external forces; the outward expansion of the QD is balanced by the restraining force exerted by the host. In the parallel PL model, we impose a Kanzaki force on each shell atom, and both the host and the core exert opposing forces. We place the corresponding shell atoms in the two corresponding models in the same positions. Therefore, the restraining force exerted by the host on each shell atom must be identical in the two cases; we note that these forces occur at the actual final position of the atoms. We denote this set of forces as $\mathbf{f}_{S,H}^{QD}$. This symbol represents generically the force on a shell atom from the host atoms and from all other shell atoms. The equality of this quantity between the two systems is expressed as

$$\mathbf{f}_{S,H}^{QD} = \mathbf{f}_{S,H}^{PL}, \tag{5}$$

Table 1. Diameters and atom counts for four multiscale models of GeSi quantum dots.

	Initial radius, unit = $a_{Si}/4$	Diameter of Ge dot along $\langle 100 \rangle$ (nm)	Inner core (atom count)	Outer core (atom count)	Shell (atom count)	Total atoms in MD model	Total atoms in supercell
Atom type			Ge	Si	Si		
Model ID							
A	4	1.1	35	246	376	657	2 000 000
B	8	2.2	281	634	840	1755	2 000 000
C	12	3.3	915	1234	1320	2149	2 000 000
F	24	6.5	7193	26 340	7796	41 329	2 000 000
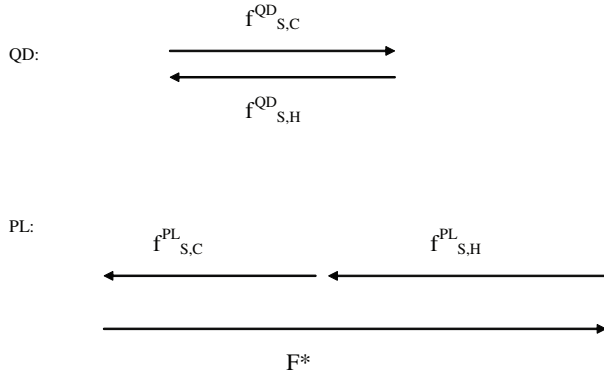
Figure 4. Illustrative force balance diagrams for individual shell atoms in the quantum dot (QD) and perfect lattice (PL) configurations. The diagrams show the relative senses and magnitudes of various force components in equations (6) and (7). The forces are generally radial, either inward or outward; the force sums illustrated apply to each vector component. Both the QD and PL sums refer to atomic arrangements similar to figure 1, but all atoms in the PL are Si. In the QD configuration, the outward force on each shell atom from the core is balanced by the restraining force from the host, as given by equation (6). For each shell atom in the PL, the Kanzaki force, $\mathbf{F}_k$, is balanced by the sum of the inward force exerted by the core, $\mathbf{f}_{S,C}^{PL}$, and the restraining force exerted by the host, $\mathbf{f}_{S,H}^{PL}$, equation (7).

where the superscript QD indicates that the actual physical forces are evaluated in the QD configuration, the first subscript, S, indicates forces on a shell atom, and the second subscript indicates the source of the forces, H for host. At the equilibrium configuration of the whole QD model, we note that for each shell atom and for each term in the column vectors of forces we must have

$$\mathbf{f}_{S,C}^{QD} + \mathbf{f}_{S,H}^{QD} = 0, \qquad (6)$$

where the second subscript indicates the source of the forces, C for core and H for host, and forces of shell atoms on other shell atoms are included with forces from the host. This equation relies on the fact that a full MD calculation with an unlimited number of atoms, or any other proper calculation method, must produce a set of atomic displacements for which the net force on each shell atom is zero.

Force balance within the PL model requires

$$\mathbf{f}_{S,H}^{PL}(\mathbf{F}^*) = -\mathbf{F}^* - \mathbf{f}_{S,C}^{PL}(\mathbf{F}^*), \qquad (7)$$

where the superscripts PL indicate the perfect lattice model, the subscripts have the same meaning as in (6) and the dependence

of the response forces on the Kanzaki force is shown explicitly. By substituting and rearranging ((5)–(7)) we may write:

$$\mathbf{F}^* = \mathbf{f}_{S,C}^{QD}(\mathbf{u}_S(\mathbf{F}^*)) - \mathbf{f}_{S,C}^{PL}(\mathbf{F}^*). \qquad (8)$$

This equation applies to each shell atom. The first term on the right is the force on a shell atom from the core atoms; it depends on the positions $\mathbf{u}_S$ (fixed for each MD run) of the shell atoms, which depend in turn on the Kanzaki force. This equation can be regarded as giving the 'output forces' on the left as a functional of the 'input forces' on the right. The solution is the set of forces for which the equation holds. The last quantity on the right is conveniently calculated numerically with the MD software before the core atoms are allowed to move, after positioning the outer core atoms by use of (1). This is a highly nonlinear equation; we solve it iteratively. At the first step, both $\mathbf{F}^*$ and $\mathbf{u}_S$ are equal to zero; the resulting value of $\mathbf{F}^*$ provides the input to the next iteration, etc.

In summary, the multiscale calculation is accomplished by combining three separate calculations: GF evaluation of the displacements of the shell and core atoms of the PL using (1), based on an estimate of the Kanzaki forces; MD evaluation of the forces on the shell atoms from the core atoms, after the displacements calculated using the GF are imposed on the starting configuration; and MD equilibration of the core atoms to their minimum energy configuration, while holding the shell atoms fixed. This calculation is iterated until (8) is sufficiently well satisfied. The convergence criterion is the match between output forces and the input forces. If the forces match, the calculation has converged and we have our Kanzaki forces. If not, a new estimate of $\mathbf{F}^*$ is made based on the mismatch between the 'input' and 'output' force in (8), and the calculation is repeated.

By the usual arguments, this force-balance configuration, between the expanding QD core and the restraining effect of the surrounding host lattice, corresponds to the minimum energy of the whole system: core, shell and host. Each successful iteration produced a closer balance between the input and output forces in (8); we were not able exactly balance the force values for each atom, partly because the MD model had a tendency to drift slightly around its energy minimum, rather than locking on to it. The uncertainty values for our final forces, estimated as the difference between input and output values of $\mathbf{F}^*$ in (8) at the final iteration, are listed below.

3.2. Procedure

In each iteration, the outer core and shell atoms are positioned using (1) with the current value of $\mathbf{F}^*$. For the first iteration, $\mathbf{F}^*$
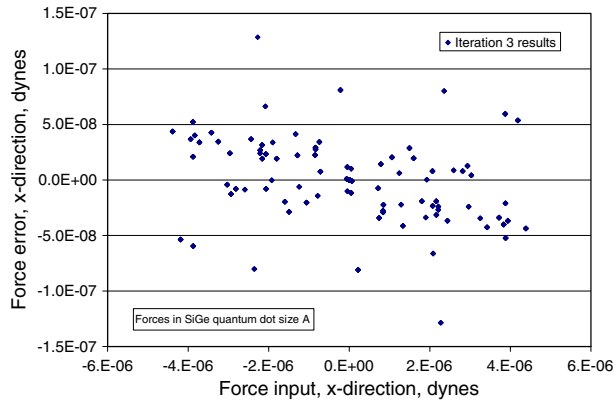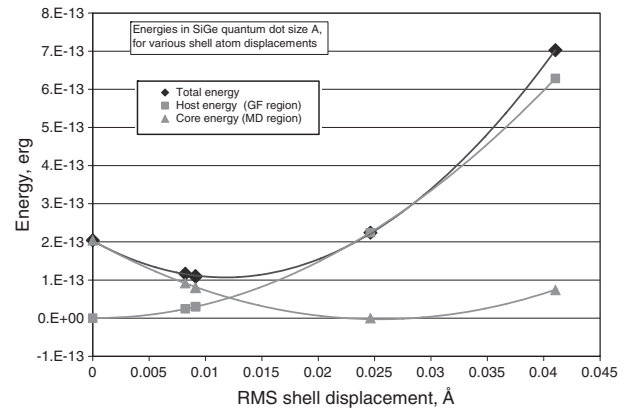
Figure 5. Force imbalance for near-converged force values in quantum dot size A, of radius 4 ($a_{Si}/4$), for iteration 3. Note that the range of magnitude of the errors (*y*-axis scale) is much smaller than the range of the forces themselves (*x* axis). For some small force values, the error is comparable to the force, but the small forces do not have a large effect on the result.

Figure 6. Total strain energies in quantum dot size A of radius 4 ($a_{Si}/4$) plotted as average energy per atom of the QD. The curves are drawn as guides for the eye. The total strain energy of the Ge–Si QD is the sum of core and host contributions. The core considered in isolation, initially placed with all atoms on Si lattice sites, reduces its energy by expanding and so reducing the compressive strain in the Ge QD. Eventually, at large expansions, the isolated core would go into hydrostatic tension and its energy would increase. For the QD-in-host system, the host is compressed radially outward by the expanding QD core and its strain energy rises. The forces on each atom are balanced at the minimum of the total energy.

is zero and all atoms are placed at perfect Si lattice positions. For all the MD runs, the shell atoms are fixed and provide the boundary condition for the MD analysis. Before the core atoms are allowed to move, the second term on the right-hand side (RHS) of (5) is calculated. Then the Ge QD proper and the inner and outer core atoms are allowed to move toward their minimum-energy positions. Several thousand MD quench steps are calculated. Two different 'quench' options were used in the MD program; in both, a specified set of atomic velocities are numerically nulled whenever a related potential energy value increases. Single-atom and full-model quenches were used. Both remove kinetic energy from the MD model, so the total energy in the model gradually decreases. We tried introducing small amounts of thermal energy to speed up convergence, followed by quenching, but this always resulted in an energy value larger than the best minimum value.

Each MD iteration provides a new value of the first term on the RHS of (8). The 'output force' is evaluated according to (8) and compared to the initial value for the current iteration. If the difference is too large, the 'output force' becomes the 'input force' for the next iteration, equation (1) is applied to find the positions of the shell and core atoms, the shell atoms are fixed at their new positions, another MD run is carried out, and so on. Perfect convergence is the condition where the 'input' forces, namely those used in (1) to position the shell atoms, are exactly equal to the 'output' forces, as given by (8).

We estimate that the individual components of our Kanzaki forces are correct within 1% of the maximum component and we expect that their combined effects are correct to within a much smaller uncertainty, because errors at individual atoms are distributed randomly. Figures 5 and 6 display sets of forces and energies plotted to show the approach to minimum overall energy for the smallest QD. Figure 5 shows the *x*-direction force error, namely the difference between output and input force value, plotted against the input force for all the shell atoms of inclusion size A. This figure shows that each individual force component has its own error. There are hundreds or thousands of these in the problems studied here. The force error plotted in figure 5 is the difference between

the 'input forces,' used in (1) to position the shell atoms, and the 'output forces,' calculated according to (8) from the MD results.

Table 2 summarizes the residual force errors. The root-mean-square (RMS) forces and force errors are given and the RMS force errors are compared with the maximum force for each QD. Table 2 shows that the errors are small compared to the maximum forces. Since the GF is linear, the maximum possible relative error in the displacements is the same as the relative error in the forces. This implies that, for all the displacements reported here, even for the small displacements at atoms located distant from the QD, the errors resulting from imperfect force matching are less than 1%.

Figure 6 shows the energy balance for inclusion size A. Energy is plotted against RMS shell atom displacement. The strain energy is made up of two main contributions, the shell-host part, based on the $\mathbf{f}_{S,H}^{PL}$ term illustrated in the PL part of figure 4 and the core-shell part, corresponding to the $\mathbf{f}_{S,C}^{QD}$ term in the MD model. The zero for the shell-host interaction energy is the energy of the Si lattice at its equilibrium lattice spacing; the shell-core interaction energy is referred to the energy of the SiGe heterostructure with no surrounding host lattice. The curves drawn in the plot are only to guide the eye. This plot shows that the total energy has a broad minimum and supports the choice of basing the convergence procedure on the force balance, as opposed to energy minimization.

4. Results

4.1. QD in infinite solid

Figure 7 shows calculated radial atomic displacements along the ⟨110⟩ direction for the four QD sizes. The displacements are taken as the difference between the final position of each atom and its initial position, which was assumed to

Table 2. Average forces and force errors for the QD models.

Quantum dot	RMS force (dyn)	RMS force error (dyn)	RMS force error /maximum force (%)
A	1.522×10^{-6}	9.98×10^{-10}	0.023
B	1.888×10^{-6}	1.71×10^{-8}	0.31
C	3.351×10^{-6}	3.58×10^{-8}	0.35
F	8.229×10^{-6}	1.04×10^{-7}	0.5
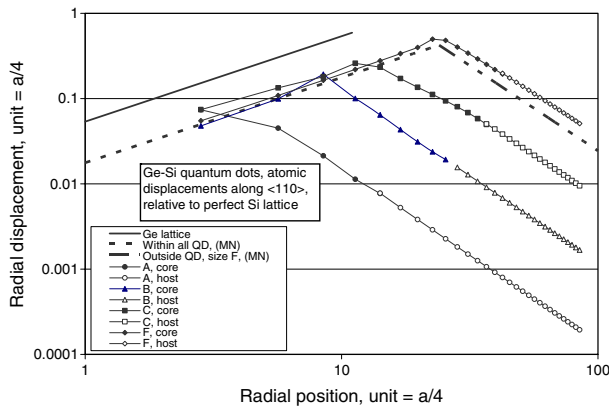
Figure 7. Plot of radial atomic displacements along the $\langle 110 \rangle$ direction around Ge–Si quantum dots in an infinite Si solid. The unit on both axes is $a_{Si}/4$. All displacements are relative to the perfect Si lattice. The curves labelled MN give Mott–Nabarro continuum solution values for comparison.
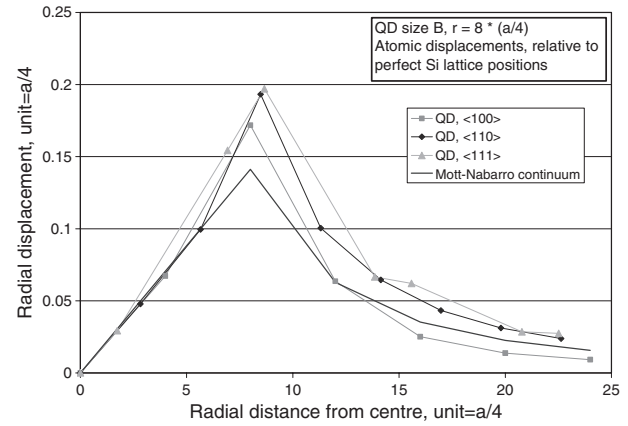
Figure 9. Atomic displacements near the Ge–Si interface, relative to perfect Si lattice positions, plotted against distance from the dot centre for quantum dot size B in the infinite solid.
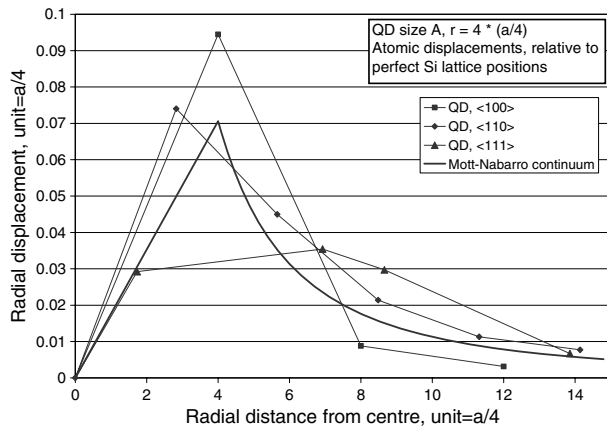
Figure 8. Atomic displacements near the Ge–Si interface, relative to perfect Si lattice positions, plotted against distance from the dot centre for quantum dot size A in the infinite solid.

be a point on the perfect Si lattice. All atomic positions and displacements are given in units of one-fourth of the diamond cubic Si lattice parameter, that is, $a_{Si}/4 = 1.358$ Å (0.1358 nm). The displacement of each atom relative to the perfect Si lattice is plotted. Atom positions in the perfect Ge lattice are shown for reference, plotted as displacements from perfect Si sites. Compressive strain within the QD moves the Ge atoms away from the perfect Ge lattice positions, given as the solid line. Ashby and Brown [38] gave a very useful statement of the Mott–Nabarro [39] estimate of displacement around a spherical inclusion. We adopt this Mott–Nabarro

(MN) result as a convenient reference, even though it is applicable specifically only to an isotropic continuum. The dashed line represents the MN solution, which is the same within all the dots; it lies below the solid line (perfect Ge positions) indicating compressive strain within the QD. The calculated atomic displacements within the dots lie above the dashed MN line and closer to the solid line. This indicates a lower compressive strain within the QD than that given by MN. The MN curve is given only for the largest QD, size F, outside the dots. In the infinite solid, the strains around the dots are compressive. Our atomic positions for this dot lie below the MN curve, indicating smaller displacements than the MN estimate. This plot shows the continuity between the GF and MD parts of the models, as well as the broad similarity between the present results and the MN results. It also shows quantitative differences between the present results and the MN estimate.

Figures 8–11 compare the atomic displacements along the $\langle 100 \rangle$, $\langle 110 \rangle$ and $\langle 111 \rangle$ directions for the four QD in the infinite solid. The atomic displacements at the Ge–Si interface are anisotropic and are larger than the reference values. The plots show the displacements in the $\langle 100 \rangle$ direction trending smaller than the MN displacements. This trend continues at larger distances, where the displacements along $\langle 100 \rangle$ are smaller than the MN values, but the displacements in $\langle 110 \rangle$ and $\langle 111 \rangle$ are larger than the MN values.

4.2. QD in semi-infinite solid

In the semi-infinite solid, the focus is on surface displacements and strains. Surface displacements calculated for the four QD sizes, buried at selected depths, are given in figures 12–15.
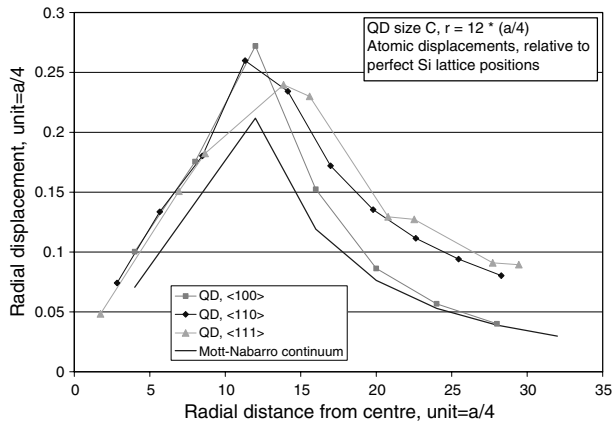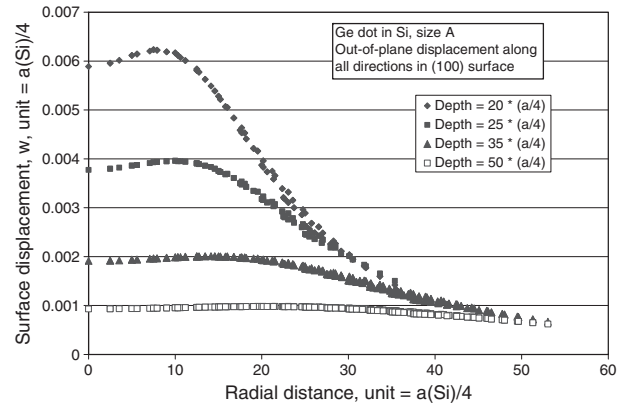
Figure 10. Atomic displacements near the Ge–Si interface, relative to perfect Si lattice positions, plotted against distance from the dot centre for quantum dot size C in the infinite solid.
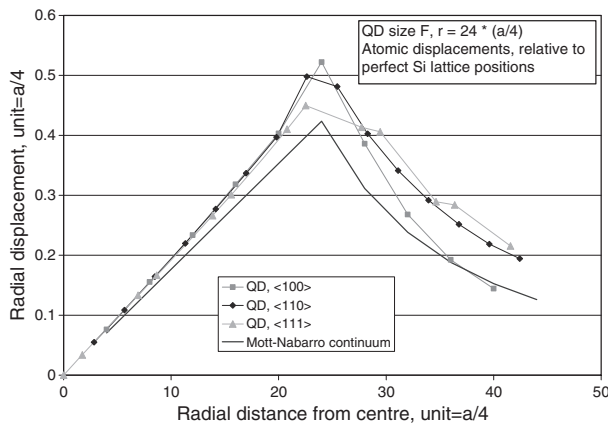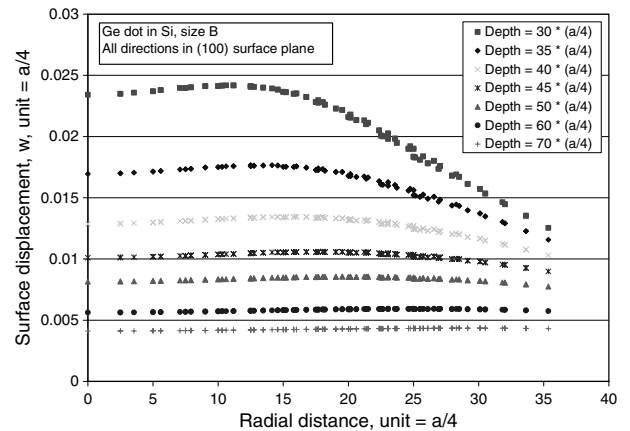

Figure 11. . Atomic displacements near the Ge–Si interface, relative to perfect Si lattice positions, plotted against distance from the dot centre for quantum dot size F in the infinite solid.

Figure 12. Out-of-plane surface displacements plotted against distance from the projection of the QD centre at the surface for QD size A. Displacements along all radial directions are plotted, giving the slight scatter in the displacements at each distance. QD depths, positions and displacements are given in units of $a_{Si}/4$.
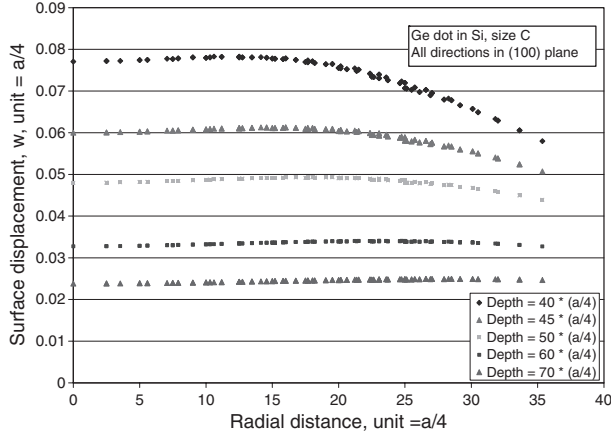

Figure 13. Out-of-plane surface displacements plotted against distance from the projection of the QD centre at the surface for QD size B. Displacements along all radial directions are plotted, giving the slight scatter in the displacements at each distance. QD depths, positions and displacements are given in units of $a_{Si}/4$.

The abscissas give distance from the projection of the centre of the QD on the surface, in units of $a_{Si}/4$. The ordinates give the out-of-plane surface displacements; the direction is outward. It can be seen from the figures that for the large dot (e.g. 6.5 nm diameter, figure 15), and perhaps even for smaller dots close to the surface, the patterns of surface displacement are of a magnitude sufficient to be observed by advanced scanned probe microscopy. The smallest QD nearest the surface produce a different pattern of out-of-plane surface displacement, namely a depression or indent at the centre of the peak, figure 12. This feature gradually decreases in magnitude as the dot size increases, and is absent in the largest dot. This feature does not occur in the continuum approximations, which are based on spherical QD, nor in the larger QD analysed here, which are more nearly spherical. The particular faceted shape of the model QD analysed is shown in figure 2. Note that no more-spherical shape is possible at this QD diameter because of the discreteness of the lattice.

　　　Figures 16–19 show the behaviour of both strain energy and diagonal components of the strain tensor for QD sizes A and F. In all these plots, the curves labelled Mindlin–Cheng [40] will be discussed below.
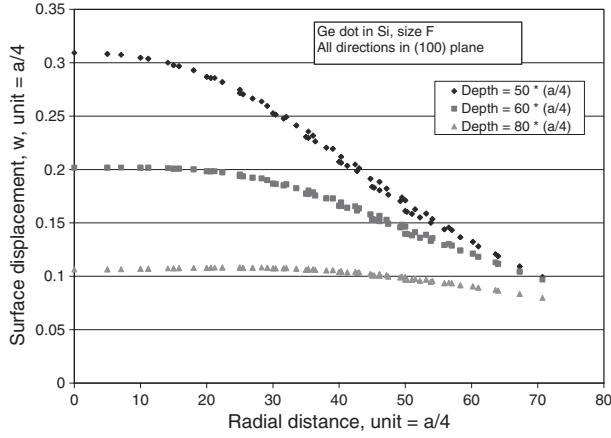
5. Discussion

In this paper we have demonstrated a multiscale modelling technique for QD and other nanoscale structures in host lattices that has four main advantages: correct treatment of the boundary conditions, with no need to impose arbitrary boundary conditions near the QD; efficient modelling of large QD, by using the GF far from the QD where the strains are small; multiscale from atomistic to continuum, with no need for arbitrary selection of joining regions or gauge lengths for strains; and efficient treatment of surface displacements and strains from buried QD. We analysed near-spherical QD because they provide a relatively simple example case. Experimentally created and observed QD are much more complicated than our model QD, in both shape and chemical composition [8]. All the atomic positions calculated for any QD would depend on its actual shape and composition. The multiscale modelling technique described here is applicable to any dot shape and composition, because we specify the starting location of each individual atom in the QD and obtain

Figure 14. Out-of-plane surface displacements plotted against distance from the projection of the QD centre at the surface for QD size C. Displacements along all radial directions are plotted, giving the slight scatter in the displacements at each distance. QD depths, positions and displacements are given in units of $a_{Si}/4$.

Figure 16. Normal strain components on the surface above QD size A, buried at a depth 20 ($a_{Si}/4$). The strain component ε_{zz} is plotted along all radial directions to show the near-isotropy. Note the local extrema in the multiscale model values for all strain components at about 8 units from the centre.
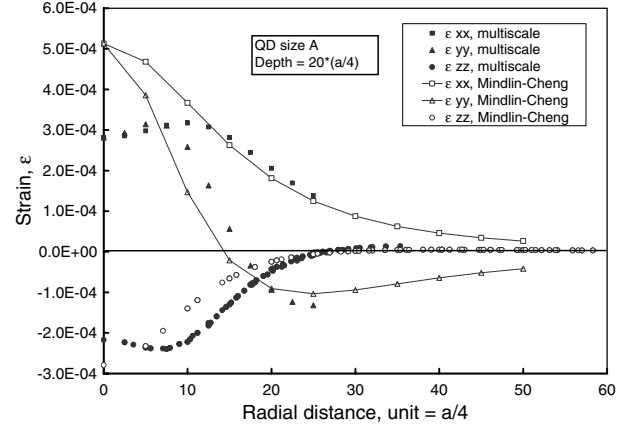

Figure 15. Out-of-plane surface displacements plotted against distance from the projection of the QD centre at the surface for QD size F. Displacements along all radial directions are plotted, giving the slight scatter in the displacements at each distance. QD depths, positions and displacements are given in units of $a_{Si}/4$.

Figure 17. Strain energy density on the surface above QD of size A, for several depths. All curves are plotted along all radial directions, to show the degree of anisotropy. Note the local extrema in the multiscale model values for all depths.

the Kanzaki forces. If more detailed observations of strain and displacement fields for QDs of specific shapes become available, the application of our method to those shapes is straightforward.
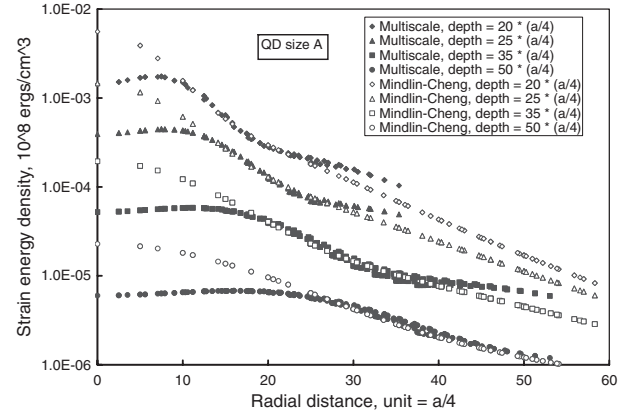
Our intent is to encourage more detailed and precise experimental measurements of such displacements and strains around QD and more refined multiscale models. The first step in this program would be to compare experimental results to a set of model results; the results given in the present manuscript are suitable for such a comparison. Such a comparison may well show that additional calculations, for different QD shapes, are needed. Such calculations can be done with the method given in this manuscript, but are outside the scope of the present study.

5.1. Atomic displacements compared to reference cases

5.1.1. Infinite solid. Atomic displacements calculated here were compared to the isotropic continuum solution of Mott
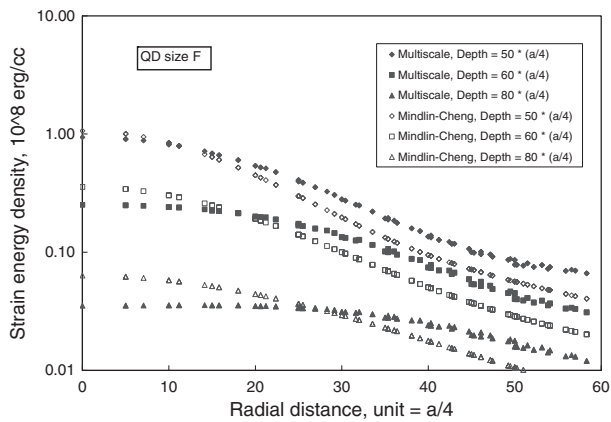
and Nabarro (MN) in figures 7–11. In all cases, the present results agree qualitatively, but not quantitatively, with the MN values. The differences in the results arise from the differences in the basic mathematical descriptions of the solid. The continuum, isotropic description of MN captures the general features, while the multiscale approach captures the effects of the anisotropic crystal lattice and the atomic interactions. The MN solution provides helpful reference values for the displacements both within and outside the QD.

5.1.2. Semi-infinite solid. Mindlin and Cheng (MC) [40] gave an expression based on isotropic continuum elasticity for surface displacements near an inclusion in a semi-infinite solid. This solution provides a reference case for the surface displacements calculated here. It has the general form of a peak located at the projection of the QD centre on the surface. Figure 20 shows ratios of surface displacements calculated here to MC values for QD size F, plotted against distance from the projection of the centre of the QD on the surface for several
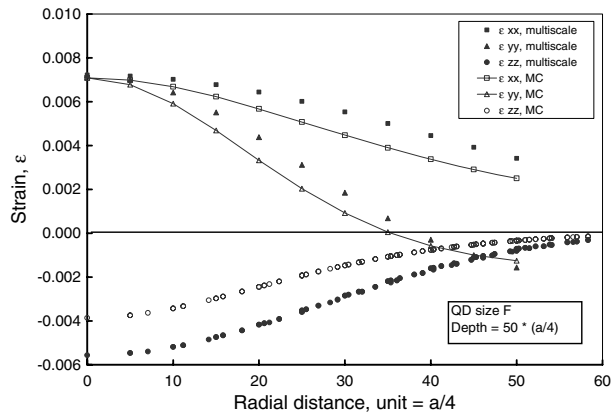
Figure 18. Normal strain components on the surface above QD size F, buried at a depth of 50 ($a_{Si}/4$). The ε_{xx} and ε_{yy} components are plotted along the (010) direction. The strain component ε_{zz} is plotted along all radial directions, to show the near-isotropy.
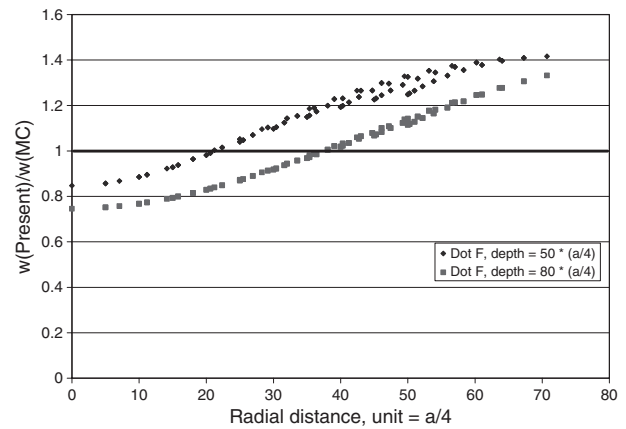

Figure 19. Strain energy density on the surface above QD size F for several depths. Data for all radial directions are included in the curves to indicate the degree of anisotropy. Note the maximum in strain energy density directly above the QD for the less-deeply-buried QD.

Figure 20. Out-of-plane surface displacements, w, relative to the Mindlin–Cheng solution for QD size F.

are as before: the isotropic continuum description captures general features, but not details for the particular materials modelled. The strain and strain energy density values show the same qualitative agreement with the MC solution as the displacements did. The local minimum at the origin in the magnitudes of all the normal strain components and the strain energy density for QD size A, see figures 16–17, are striking deviations of the present results from the MC solution. The differences between the present results and the MC solution can be attributed to:

(i) the discrete structure of the lattice in and around the QD;
(ii) the exact shape of the QD, which is rhombohedral in our model and is spherical in the MC solution; and
(iii) the assumption of isotropy in the MC model, in contrast to our multiscale model that accounts for full elastic anisotropy.

5.2. Previous calculations for Ge–Si

Calculations of the displacements around Ge–Si QD of various types have been reported previously in the literature. The closest in spirit to the present work is that of Makeev and Madhukar [17]. Their fully atomistic calculation used a different interatomic potential, and they reported results in terms of stresses and strains. Their MD calculation included a free surface, but without modifying the potential at the surface, as was done for example by Vashishta *et al* [44] for GaAs surfaces, and without allowing the surface to reconstruct. Their extraction of stress and strain values from atomic displacements required a choice of the definitions used. Here we treat the surface in the continuum approximation, using the continuum GF as the asymptotic limit of the LGF. No choices of definitions need be made in taking this limit. Our atomistic treatment extends much further into the substrate. The present results, like those of [17], reproduce the general scaling of the previous elasticity solutions by Mott and Nabarro [39] and Mindlin and Cheng [40]. These results all show that the free surface above a Ge QD in Si is displaced out of plane, in a direction away from the QD, meaning that the QD produces a broad peak on the surface.

The present results indicate that small, faceted QD placed below the free surface would have a distinctive feature if

radial distances. The curves lie near a value of 1, indicating broad agreement between the present solution and the MC result. However, the present results are less than the MC values directly above the QD, even for QD size F. The MC results have no indent at the centre of the peak, in contrast to the present results for the smaller dots.

The usefulness of the Green's function in describing anisotropic semiconductors has been discussed in detail in the literature [28, 41–43]. The elastic anisotropy of the Si and Ge produces the visible scatter of the curve in figure 20 for depth = $50(a_{Si}/4)$. However, at the radial distance where this anisotropy becomes visible, the absolute value of the surface displacement, shown in figure 15, is well below its maximum value. Only the flanks of the peak have noticeable anisotropy, while the peak itself is essentially symmetric.

Strains and strain energy densities at the surface of a semi-infinite Si solid above a buried Ge QD were plotted in figures 16–19, along with curves given by the MC solution. As for the displacements, the agreement between the present results and the MC solution is qualitative only. The reasons

Table A.1. Parameters for the MEAM interatomic potential used here. E_{sub} in eV, r_{nn} in ångstroms, remainder dimensionless. The nomenclature is the same as in [30].

					Parameter							
Interaction	E_{sub} (eV)	r_{nn} (Å)	α	A	$\beta^{(0)}$	$\beta^{(1)}$	$\beta^{(2)}$	$\beta^{(3)}$	$t^{(0)}$	$t^{(1)}$	$t^{(2)}$	$t^{(3)}$
Si–Si	4.63	2.35	4.87	0.84	3.6	5.5	5.5	4.5	1.0	5.6	8.9	−2.50
Ge–Ge	3.85	2.45	4.98	0.92	4.2	5.5	5.5	3.9	1.0	4.4	6.7	−1.20
Si–Ge	4.24	2.401	4.92	NA								

observed by scanned-probe microscopy, that is, an indent or dimple on top of its displacement peak. This dimple diminishes as the QD radius increases from 4 to 12 $a_{Si}/4$, and is not reported in [17]. This feature is somewhat similar to the result of Zhang *et al* [45]. Zhang *et al* report a minimum strain directly above their QD centre for a near-surface buried dot, that is, depth is less than the dot half-width. They found high surface strains in a nearly rectangular locus directly above the perimeter of their buried rectangular QD, which formed a direct one-to-one projection of the perimeter of their QD onto the specimen surface. Our results, figure 12, are far-field, since the depth is 2.5 times the dot diameter. Our (relatively) high surface displacements, and also high strains, form a nearly circular locus with a diameter of about 3.5a, where a is the lattice parameter. However, the perimeter of our QD forms a square of side $\sqrt{2}a$ in the x–y plane, with its vertices at the $\langle 100 \rangle$ directions. In addition, the top side of our smallest QD actually has the form of a square pyramid (as does the bottom side). Thus, the locus of maximum strains and displacements in the surface is not a simple projection of the QD shape, and this locus has a diameter different from the QD size. Both the strain energy at the surface and the hydrostatic strain, given as the trace of the strain tensor, reveal similar patterns of spatial dependence. A key point is that the hydrostatic strain at the surface is tensile [17], in contrast to the strain in the infinite solid near the QD.

Tersoff *et al* [46] gave a simple model for estimating the tendency for self-alignment of an added layer of QD on top of an existing layer, based on the surface strains. They said that the favoured growth should 'reduce the mismatch'. We have calculated surface strains and strain energy densities. These are shown in figures 16 and 17 for two QD. The strains at the surface are all tensile. The Ge atom is larger than the Si atom, so a Ge atom incorporated into a tensile strain field should reduce the mismatch. If we consider the larger QD, figure 17, we see that the maximum of tensile strain is directly above the QD. The situation is different for the small QD, for which the strain energy and strain components are plotted in figure 16. In this situation, the maximum strain is not directly above the existing QD, but is offset.

So, based on the model of [46], one would suspect that growth of vertical arrays should break down, or be less favoured, for very small QD close to the surface. For the QD modelled here, the crossover size to the behaviour where vertical growth is favoured is complete by a dot diameter of 6.5 nm (65 Å). However, the numerical mismatch in figure 16 between the maximum and the central minimum, though numerically significant within the present model, may not be large enough to support this conclusion for real cases. As pointed out by Tersoff *et al* [46], accurate predictions of QD array formation would require more sophisticated

computations; these could be calculations of the elastic interaction energy between dots or of the elastic energy release rate [47], which are beyond the scope of the present paper. The curves in figures 16 and 17 are sensitive to the shape of the QD. Our results for polyhedral QDs should serve as a good approximation for the {105}-faceted QDs, similar to those analysed by Daruka *et al* [13] in the InAs/GaAs system. The behaviour may be different for pyramidal and other shapes. For example, the stress field from a {101}-faceted pyramidal island falls off as 1/h for small values of h, where h is the depth of the quantum dot below the free surface [48]. Our results will not be, therefore, applicable to these QDs.

5.3. Limitations of the method

We used an empirical interatomic potential function. An *ab initio* treatment of the atomic interactions would remove the necessity for assuming an interatomic potential. We treated the surface in the harmonic approximation, without considering surface reconstruction and without altering the interatomic potential.

Acknowledgments

Appendix. Numerical values for force calculations

The interatomic force constant matrices [49] for first and second neighbours in a perfect Si lattice are written as follows:

$$\Phi(0; 1, 1, 1) = -\begin{pmatrix} \alpha & \beta & \beta \\ \beta & \alpha & \beta \\ \beta & \beta & \alpha \end{pmatrix} \qquad (A.1)$$

$$\Phi(0; 2, 2, 0) = -\begin{pmatrix} \mu & \nu & \delta \\ \nu & \mu & \delta \\ -\delta & -\delta & \lambda \end{pmatrix} \qquad (A.2)$$

where the atomic coordinates are written in units of $a/4$. The force constants are evaluated numerically from the MEAM potential using the parameters given in table A.1. For this potential, the force constants are zero beyond the second neighbours. Numerical values of the constants in equations (A.1) and (A.2) are given below in units of 10^4 dynes cm^{-1}:

$$\alpha = 19.512, \qquad \beta = 15.510, \qquad \lambda = 0.576,$$
$$\mu = -1.325, \qquad \nu = -1.377, \qquad \delta = 1.628.$$

These constants are used in the calculation of the perfect lattice Green's function for a supercell consisting of 10^6 unit cells or 2×10^6 Si atoms using the Fourier transform technique [25].

References

[1] Imamoglu A 2003 *Physica* E **16** 47–50
[2] Tillmann K and Jager W 2000 *J. Electron Microsc.* **49** 245–57
[3] Woll A R, Rugheimer P and Lagally M G 2002 *Mater. Sci. Eng.* B **96** 94–101
[4] Ruda H E and Qiao B 2003 *Proc. IEEE* **91** 1874–83
[5] Stangl J, Holy V and Bauer G 2004 *Rev. Mod. Phys.* **76** 725–83
[6] Tahan C, Friesen M and Joynt R 2002 *Phys. Rev.* B **66** 035314
[7] Golovach V N, Khaetskii A and Loss D 2004 *Phys. Rev. Lett.* **93** 016601
[8] Chaparro S A, Drucker J, Zhang Y, Chandrasekhar D, McCartney M R and Smith D J 1999 *Phys. Rev. Lett.* **83** 1199–202
[9] Konchenko A, Nakayama Y, Matsuda I, Hasegawa S, Nakamura Y and Ichikawa M 2006 *Phys. Rev.* B **73** 113311
[10] Grundmann M, Stier O and Bimberg D 1995 *Phys. Rev.* B **52** 11969–81
[11] Nenashev A V and Dvurechenskii A V 2000 *J. Exp. Theor. Phys.* **91** 497–503
[12] Andreev A D, Downes J R, Faux D A and O'Reilly E P 1999 *J. Appl. Phys.* **86** 297–305
[13] Daruka I, Barabasi A L, Zhou S J, Germann T C, Lomdahl P S and Bishop A R 1999 *Phys. Rev.* B **60** R2150–3
[14] Kikuchi Y, Sugii H and Shintani K 2001 *J. Appl. Phys.* **89** 1191–6
[15] Makeev M A and Madhukar A 2001 *Phys. Rev. Lett.* **86** 5542–5
[16] Kohler C 2003 *J. Phys.: Condens. Matter* **15** 133–46
[17] Makeev M A and Madhukar A 2003 *Phys. Rev.* B **67** 073201
[18] Tadmor E B, Ortiz M and Phillips R 1996 *Phil. Mag.* A **73** 1529–63
[19] Tewary V K and Read D T 2004 *Comput. Model. Eng. Sci.* **6** 359–71
[20] Rao S, Hernandez C, Simmons J P, Parthasarathy T A and Woodward C 1998 *Phil. Mag.* A **77** 231–56
[21] Yang B and Tewary V K 2005 *Int. J. Solids Struct.* **42** 4722–37
[22] Tersoff J 1988 *Phys. Rev.* B **38** 9902–5
[23] Cormier J, Rickman J M and Delph T J 2001 *J. Appl. Phys.* **89** 99–104
[24] Tewary V K 2004 *Phys. Rev.* B **69** 094109
[25] Tewary V K 1973 *Adv. Phys.* **22** 757–810
[26] Maradudin A A, Montroll E W and Weiss G H 1971 Ipatova theory of lattice dynamics in the harmonic approximation *Solid State Physics* ed H Ehrenreich, F Seitz and D Turnbull (New York: Academic)
[27] Kanzaki H 1957 *Phys. Chem. Solids* **2** 24
[28] Ting T C T 1996 *Anisotropic Elasticity* (Oxford: Oxford University Press)
[29] Kim K M, Park Y J, Son S H, Lee S H, Lee J I, Park J H and Park S K 2004 *Physica* E **24** 148–52
[30] Baskes M I 1992 *Phys. Rev.* B **46** 2727–42
[31] Baskes M I 1997 *Mater. Chem. Phys.* **50** 152–8
[32] Cherne F J, Baskes M I and Deymier P A 2002 *Phys. Rev.* B **65** 024209
[33] Yin M T and Cohen M L 1982 *Phys. Rev.* B **26** 5668–87
[34] Bernstein N, Mehl M J, Papaconstantopoulos D A, Papanicolaou N I, Bazant M Z and Kaxiras E 2000 *Phys. Rev.* B **62** 4477–87
[35] Bernstein N, Mehl M J and Papaconstantopoulos D A 2002 *Phys. Rev.* B **66** 075212
[36] Sitch P K, Frauenheim T and Jones R 1996 *J. Phys.: Condens. Matter* **8** 6873–88
[37] Rifkin J 2002 *XMD software* (Computer Program)
[38] Ashby M F and Brown L M 1963 *Phil. Mag.* **8** 1083–103
[39] Mott N F and Nabarro F R N 1940 *Proc. R. Soc.* **52** 86–9
[40] Mindlin R D and Cheng D H 1950 *J. Appl. Phys.* **21** 931–3
[41] Pan E and Yang B 2001 *J. Appl. Phys.* **90** 6190–6
[42] Pan E 2003 *J. Appl. Mech.-Trans. ASME* **70** 180–90
[43] Pan E 2002 *J. Appl. Phys.* **91** 6379–87
[44] Su X T, Kalia R K, Nakano A, Vashishta P and Madhukar A 2003 *J. Appl. Phys.* **94** 6762–73
[45] Zhang J J, Zhang K W and Zhong J X 2004 *Appl. Phys. Lett.* **84** 1853–55
[46] Tersoff J, Teichert C and Lagally M G 1996 *Phys. Rev. Lett.* **76** 1675–8
[47] Yang B and Tewary V K 2003 *Phys. Rev.* B **68** 035301
[48] Denker U, Stoffel M and Schmidt O G 2003 *Appl. Phys. Lett.* **83** 1432–4
[49] Herman F 1959 *Phys. Chem. Solids* **8** 405–18